Synergistic Surface Modification of Tin–Lead Perovskite Solar Cells

Shuaifeng Hu, Pei Zhao, Kyohei Nakano, Robert D. J. Oliver, Jorge Pascual, Joel A. Smith, Takumi Yamada, Minh Anh Truong, Richard Murdey, Nobutaka Shioya, Takeshi Hasegawa, Masahiro Ehara, Michael B. Johnston, Keisuke Tajima, Yoshihiko Kanemitsu, Henry J. Snaith, and Atsushi Wakamiya**

S. Hu, Dr. J. Pascual, Dr. T. Yamada, Dr. M. A. Truong, Dr. R. Murdey, Dr. N. Shioya, Prof. T. Hasegawa, Prof. Y. Kanemitsu, Prof. A. Wakamiya
Institute for Chemical Research, Kyoto University, Gokasho, Uji, Kyoto 611-0011, Japan.
E-mail: wakamiya@scl.kyoto-u.ac.jp

Dr. P. Zhao, Prof. M. Ehara
Research Center for Computational Science, Institute for Molecular Science, Okazaki, 444-8585, Japan.

Dr. K. Nakano, Prof. K. Tajima
RIKEN Center for Emergent Matter Science (CEMS), Wako, Saitama 351-0198, Japan.

Dr. R. D. J. Oliver, Dr. J. A. Smith, Prof. M. B. Johnston, Prof. Henry J. Snaith
Clarendon Laboratory, Department of Physics, University of Oxford, Oxford OX1 3PU, U.K.
E-mail: henry.snaith@physics.ox.ac.uk

Keywords: solar cell, perovskite, interfacial chemistry, surface defect, coordination

Interfaces in thin-film photovoltaics play a pivotal role in determining device efficiency and longevity. Herein, we study the top surface treatment of mixed tin–lead (~1.26 eV) halide perovskite films for p-i-n solar cells. We are able to promote charge extraction by treating the perovskite surface with piperazine. This compound reacts with the organic cations at the perovskite surface, modifying the surface structure and tuning the interfacial energy level alignment. In addition, the combined treatment with C_{60} pyrrolidine tris-acid (CPTA) reduces hysteresis and leads to efficiencies up to 22.7%, with open-circuit voltage values reaching 0.90

V, ~92% of the radiative limit for the band gap of this material. The modified cells also show superior stability, with unencapsulated cells retaining 96% of their initial efficiency after >2000 hours of storage in N_2 and encapsulated cells retaining 90% efficiency after >450 hours of storage in air. Intriguingly, CPTA preferentially binds to Sn^{2+} sites at film surface over Pb^{2+} due to the energetically favoured exposure of the former, according to first-principles calculations. This work provides new insights into the surface chemistry of perovskite films in terms of their structural, electronic, and defect characteristics and we use this knowledge to fabricate state-of-the-art solar cells.

1. Introduction

Metal halide perovskites are promising materials for developing high-performance and cost-effective photovoltaics, owing to their strong optical absorption, tunable bandgap, and solution-processable fabrication protocols.[1-3] Within only about one decade, the efficiency of single-junction perovskite solar cells (PSCs) has surpassed 25%, for devices fabricated in both n-i-p (regular)[4-6] and p-i-n (inverted)[7-8] structures, on par with state-of-the-art crystalline silicon solar cells.[9] However, the light-harvesting performance of perovskite photovoltaic devices is still restricted by imperfect surfaces, which display heterogeneities in structural and semiconducting characteristics.[10-12]

For inverted PSCs, which show advantages for manufacturing, the interfaces interconnecting the perovskite with the charge extraction layers are of utmost importance for both efficiency and longevity.[13-16] For example, Li et al.[17] recently improved the stability and efficiency (>24%) of lead PSCs by constructing heterojunctions via surface sulfidation. Azmi et al.[18] fabricated damp heat-stable PSCs by tailoring the dimensional fragments of two-dimensional (2D) perovskite layers formed with oleylammonium iodide. Again, by functionalizing the lead halide perovskite top interface and electron-extraction properties with a ferrocene derivative, Li et al.[7]

simultaneously enhanced the stability and efficiency of inverted PSCs, with power conversion efficiency (PCE) values up to 25%.

Mixed tin–lead (Sn–Pb) perovskites with a narrow optical gap of ~1.2 eV[19-20] are crucial materials for use in multi-junction all-perovskite tandem cells,[21-22] to surpass single-junction efficiency limitations[23] in a cost-effective manner.[24] Appropriate top interface modifications are even more crucial for mixed Sn–Pb materials,[22, 25-26] given the facile oxidation of Sn^{2+},[27-28] especially at the film surface,[29] and the regularly substandard quality of films resulting from the rapid crystallization.[30-31] Wei et al.[32] introduced trace phenethylammonium (PEA^+) cations at the perovskite film surface and grain boundaries in the anti-solvent quenching step. By deliberately avoiding the excess formation of 2D phases that impede charge extraction in inverted architecture devices,[33] the authors achieved PCEs of 19.4% and 23.5% for the single-junction mixed Sn–Pb PSCs and monolithic all-perovskite tandem cells, respectively. Instead of using ammonium cations,[34-35] Kapil et al.[36] demonstrated that a neutral amine, ethylenediamine (EDA), can lower the surface defect density and protect the perovskite from oxidation by chelating with tin at the surface. As a result, they achieved a PCE of up to 21.7% with mixed Sn–Pb PSCs. Recently, our group established that charge carrier extraction can be greatly enhanced by individually introducing ammonium-functionalized molecules, ethylenediammonium diiodide ($EDAI_2$), and glycine hydrochloride (GlyHCl), to the top and buried interfaces, respectively, for inverted mixed Sn–Pb cells.[37] We accordingly achieved the record efficiency of 23.6%. The roles shared by the amine and ammonium treatments and the differences between them, however, are yet to be unveiled. In addition, unraveling the structural and electronic features of the surface of mixed Sn–Pb films (e.g., from the viewpoint of perovskite defect chemistry) is pivotal for enhancing the efficiency of single-junction mixed Sn–Pb PSCs and all-perovskite tandem cells further.[21]

Herein, we report a simple post-treatment strategy for mixed Sn–Pb perovskite films for achieving efficient and stable solar cell devices. The method was designed to simultaneously

tune the electronic properties and passivate defect states at the film surface. As such, this treatment synergistically enhanced charge carrier extraction and reduced trap-assisted recombination. Specifically, we realized that post-applied diamines preferentially protonate to the corresponding diammonium via *in situ* reaction with the organic cation(s) at the surface, originating from the grain boundaries and/or perovskite grain surface. Meanwhile, we found that the diammoniums are able to reconstruct the perovskite surface fragments by locating at an A-site in the perovskite lattice and/or serving as a spacer to split the inorganic octahedral slabs, forming lower dimensional perovskite structures. At the same time, the energy levels of the treated films at the surface are tuned to be more favorable for electron transport, leading to efficiency enhancement of the cells. To mitigate the remaining hysteresis in the devices, we combined the diamine treatment with a fullerene derivative, C_{60} pyrrolidine tris-acid (CPTA). The carboxylic acid functionalities of the fullerene can passivate the surface further. The cells resulting from the synergistic strategy show further enhanced efficiencies, greatly suppressed hysteresis, and significantly extended device longevity. Furthermore, we also found that the iodide vacancies are energetically more favored when formed at the octahedral units centered with Sn than with Pb, according to first-principles calculations. In this sense, this is likely to be one of the main origins of the particularly strong potential for interface engineering in Sn-containing perovskite films. Therefore, this work presents a robust interface engineering strategy for the fabrication of efficient and stable mixed Sn–Pb PSCs, while introducing a new understanding of mixed Sn–Pb perovskite surfaces, critical to enable further understanding and development of these materials.

2. Results and discussion

2.1. Amine to ammonium via *in situ* reaction at the surface

The selected diamines are piperazine (PP), 4-aminopiperidine (4APP), and 4-(aminomethyl)piperidine (4AMP), as they possess similar structures where only the carbon chain of one of the amines varies in length (as seen in **Figure 1a**). Firstly, we aim to verify the reaction of the diamines with the organic cation(s) comprising the perovskite material. For this, we conducted ^{1}H nuclear magnetic resonance (NMR) characterization, the results of which are shown in **Figure S1–3**. We mixed the diamines individually with formamidinium iodide (FAI) in a molar ratio of 1:2 in DMSO-d_6, and the solutions were heated at 70 °C for 30 min with vigorous stirring. From the spectra, FA^+ presents three noticeable proton signals: the peak at δ = 7.86 ppm is assigned to the proton bonded to the center carbon, while the other two peaks centered at 8.63 and 8.95 ppm belong to the protons from the amine and ammonium groups of FA^+, respectively. With the addition of the diamines, however, the two peaks from the nitrogen atoms of pristine FA^+ are strongly attenuated. One new sharp peak is formed at δ = 6.49, 6.06, and 5.97 ppm for FA^+ mixed with PP, 4APP, and 4AMP, respectively. This new peak originates from the protons bonded with the nitrogen atoms of both FA^+ and diamines. The upfield shift of the proton signals from FA^+ is caused by the strong shielding of its ammonium moiety by the diamines.[38] Since the diamines are stronger bases than FA^+, this proton transfer reaction is highly favored, suggesting that this Brønsted–Lowry acid-base reaction likely also occurs at the perovskite film surface.

To verify this, we applied the diamines on the perovskite films with the composition of $Cs_{0.1}FA_{0.6}MA_{0.3}Sn_{0.5}Pb_{0.5}I_3$ (MA is methylammonium). Tin(II) fluoride (SnF_2), ammonium thiocyanate (NH_4SCN), and GlyHCl were included in the precursor solution as additives based on our previous investigation.[37] The fabrication protocols of the films are provided in the supporting information. To obtain crystallographic and morphological information, we characterized the pristine films and the films post-treated with PP, its iodide salt piperazine-1,4-diium iodide (PPI_2), 4APP, and 4AMP using X-ray diffraction (XRD), 2D grazing-incidence wide-angle X-ray scattering (2D GIWAXS), scanning electron microscopy (SEM),

and atomic force microscopy (AFM). In these cases, the treated films were prepared by dissolving 0.5 mg of the diamines in 1 mL IPA/toluene (1/1, v/v) mixed solvent and individually coated on the surface of freshly-fabricated perovskite films. From the 2D GIWAXS and XRD patterns, shown in **Figure 1b,** between the pristine (denoted as 'w/o') and treated films several differences are observed. For all treatments, we find a partial reorientation of the perovskite phase (**Figure S4–6**), indicative of improved crystallinity at the surface, and small changes in the intensity of PbI_2 scattering (**Figure S7**). For the films treated with 4APP and 4AMP, however, we clearly observed low dimensional phases oriented in-plane and out-of-plane, respectively. The new phases have the scattering vector (*q*-value) of 0.72 (4APP) and 0.60 (4AMP) $Å^{-1}$, corresponding to 2θ values of 10.14° and 8.45°, respectively. Comparing the XRD patterns of our films and those simulated from published single crystal data,[39] it can thus be concluded that Dion-Jacobson (DJ) phase 2D-layered perovskites with $n = 1$ were formed at the surface of the 4AMP-treated films (**Figure S8**), implying the protonation of the diamine to diammonium. In the case of 4APP, we refined the crystal structure with diffraction data acquired from a single crystal, synthesized with the conventional solution method given in supporting information. A comparison suggested that the in-plane-oriented low-dimensional species formed at the surface of the 4APP-treated films is a 0D phase, $(4APP)_2PbI_6$, (**Table S1, Figure S9**). This again indicates the protonation of the diamine to diammonium at the perovskite film surface. Thus, due to the similarity in their structures and chemical properties as learned from ^1H NMR, we suggest a similar process of protonation of the diamine is likely to occur in the PP-treated films, even though no structural change was detected, presumably owing to a higher formation energy of such a phase. Regarding the conversion of amine to ammonium in perovskite organic materials, similar processes have also been previously observed.[38, 40-41] Accordingly, we conclude that the amine bases applied to the perovskite film surface will be protonated to the corresponding ammonium cations by reacting with the organic cation(s), e.g., FA^+, MA^+, and NH_4^+ at the perovskite grain boundaries and/or lattice at the

surface region. At the same time, the newly-formed cations reconstruct the perovskite structures at the surface *in situ*, in some cases generating new phases with lower dimensionality (i.e., 0D and 2D in the case of 4APP and 4AMP, respectively), along with drastic changes in the morphology evident in **Figure 1c and S10–12**, while there are no obvious changes in the optical absorption characteristics (**Figure S13**). The starkest difference in morphology is with the 4APP and 4AMP cases, with 4APP treatment leading to surface crystallites in **Figure 1b**, most likely domains of the newly introduced 0D phase. The surface of the 4AMP treated film appears to have less well-defined grain boundaries, consistent with a complete surface coating of a new phase.

To gain further information on the electronic structure of the films, we conducted ultraviolet photoelectron spectroscopy (UPS) measurements (**Figure 1d and S14**). From the results, we observed that the vacuum levels of the films treated with PPI_2, PP, 4APP, and 4AMP are shifted to deeper energies by 0.23, 0.20, 0.25, and 0.31 eV, respectively, compared to the pristine perovskite films. This suggests the formation of a surface dipole after the application of the diamines and their subsequent protonation at the film surface, in line with our previous results.[37] In comparison with the pristine perovskite films, we also found a notable deepening of the valence band maximum (VBM) by 0.17, 0.11, 0.20, and 0.20 eV for the films treated with PPI_2, PP, 4APP, and 4AMP, respectively. Thus, two benefits can be obtained from the post-treatments. One is that the surface dipole creates an electric field,[42] which will assist in driving the electrons to the electron extraction layer. The other is that the deeper VBM at the surface will prevent photogenerated holes from reaching the electron extraction layer,[43] leading to a further decrease in charge carrier recombination events at the interface. Therefore, an enhancement of the resultant solar cell performance can be anticipated.

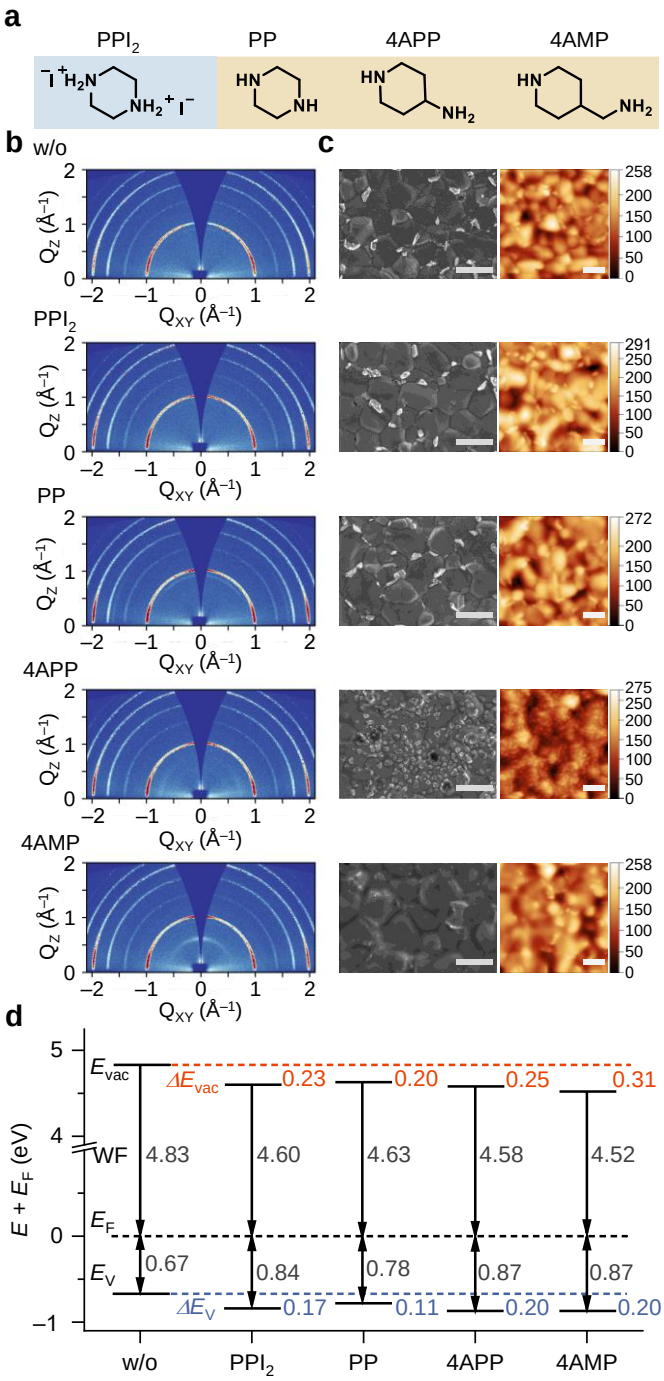

Figure 1. Film characterizations. **a,** Chemical structure of PPI_2, PP, 4APP, and 4AMP. **b,** 2D GIWAXS patterns probed at a grazing incidence angle of 0.4° for the films processed without treatment (w/o) and treated with PPI_2, PP, 4APP, and 4AMP, respectively. The partial scattering ring at $q = 0.9$ Å^{-1} originates from residual PbI_2 in the films, the corresponding 1D XRD patterns are also provided in **Figure S7**. **c,** SEM (left) and AFM (right, values in height scale bar are given in nm) images viewed from the top of the films (scale bar: 1 μm), cross-section SEM

images, topographic AFM images, and surface roughnesses are provided in the supporting information (**Figure S10–12**). **d,** Energy level diagram of pristine (w/o) and post-treated perovskite films. E_{vac} (vacuum level) and E_V (valence band maximum) are shown aligned at the Fermi level, E_F. ΔE_{vac} and ΔE_V are the difference of energies in vacuum level and valence band maximum between the treated and untreated films. The UPS spectra are given in the supporting information (**Figure S14**).

To verify the effectiveness of the surface treatment, we fabricated solar cells with perovskite films treated with the different diamines, using an inverted device architecture: FTO/PEDOT:PSS/perovskite/C_{60}/BCP/Ag, where PEDOT:PSS is poly(3,4-ethylenedioxythiophene):poly(styrene-sulfonate) and BCP is bathocuproine. The designated cell active area is 0.0985 cm^2 and current density–voltage (*J–V)* curves were measured under simulated AM1.5 G illumination. The best PCE of 20.8%, with an open-circuit voltage (V_{OC}) of 0.86 V, was obtained for the cells fabricated with PP treatment, the champion *J–V* curves are shown in **Figure S15**. Likewise, the cells treated with its ammonium salt, PPI_2, also presented a high PCE of 19.4% with a similar V_{OC} up to 0.85 V. We also observed an almost identical enhancement of the V_{OC} for the cells treated with 4APP and 4AMP, though the short-circuit current density (J_{SC}) and fill factor (*FF*) were decreased. These downsides are likely caused by i) partial erosion of the films by the diamines, due to their stronger basicity compared to PP (**Figure S10**), as evident from the morphological characterizations above; ii) an energy barrier created by the newly-formed low-dimensional phases. In summary, we observed an increase in the V_{OC} of ~40 mV for the devices treated with the examined diamines, validating the observations from the film characterizations above. Both treated and untreated devices still showed a significant *J–V* hysteresis, however.

2.2. Synergistic modification for well-performing PSCs

To reduce the *J–V* hysteresis,[44] we included an additional component at the perovskite surface. Fullerene derivatives have been extensively employed owing to their notable ability to reduce charge accumulation and passivate the defects located at surfaces and grain boundaries of the perovskite films.[45-49] CPTA was selected to be applied together with PP in the post-treatment solution, as it contains three carboxyl groups, which can potentially interact with under-coordinated metal centers in the perovskite films. To examine the acid-base reaction between PP and CPTA, we performed ^{1}H NMR measurements. From the NMR spectra, shown in **Figure S16**, we observed that the adjacent protons from PP shifted from 2.59 to 2.73 ppm when mixed with CPTA, indicating that an acid-base reaction occurred between PP and CPTA.

To verify the effects of the proposed modification, we compared solar cells treated with PP and PPCPTA with the untreated reference, where PPCPTA denotes a mixture of PP and CPTA. Experimental details and SEM images of the films are provided in the supporting information in **Figure S17**. The cells were fabricated and characterized with the same protocols mentioned above. A schematic of the device architecture and cross-sectional SEM image are provided in **Figure 2a**. The *J–V* curves and cell parameters were drawn from devices made in the same batch for accurate comparison (**Figure 2b, Table 1**). For the reverse scan, the best performance of the control device was 17.7% (V_{OC} = 0.81 V, J_{SC} = 30.6 mA cm^{-2}, and *FF* = 0.72). The PP-treated cells had a PCE of 20.2% (V_{OC} = 0.86 V, J_{SC} = 30.8 mA cm^{-2}, and *FF* = 0.76). Meanwhile, for the PPCPTA-treated device, a champion PCE of 22.3% was achieved (V_{OC} = 0.88 V, J_{SC} = 31.2 mA cm^{-2}, and *FF* = 0.81). The V_{OC} was enhanced even further, together with J_{SC} and *FF*, indicating reduced defect densities and well-facilitated charge extraction at the modified surface. The stabilized power output is shown in **Figure 2c**, with a PCE of 21.8% after 120 s of continuous measurement. The PPCPTA-treated devices showed negligible hysteresis ($PCE_{fwd.}$: 22.0%, $PCE_{rev.}$: 22.3%), suggesting reduced charge accumulation and/or suppressed interaction with mobile ions.[50-52] Cell parameters also present very narrow

distributions (**Figure S18)**. In comparison with the untreated ones, the cells treated with only CPTA show a slight performance improvement, with the contribution mainly coming from an enhanced V_{OC}, along with reduced hysteresis (**Figure S19**). This illustrates that the combined PPCPTA surface modification has a greater effect than either of the individual modifications. Given the well-known reproducibility issues for Sn-containing PSCs, we also fabricated cells incorporating the PPCPTA treatment over three months (**Figure 2d**), with average PCE values of 21.10 ± 0.67%, 20.07 ± 0.72%, and 21.61 ± 0.40%, respectively, indicating the reproducibility of the post-treatment method. Using the optimal conditions, we obtained the best PCE values in March, reaching up to 22.7% with no hysteresis (**Figure S20**), representing one of the highest efficiencies for the cells with a ~1.26 eV band gap based on present reports.[53-59] As shown in **Figure 2e**, the highest external quantum efficiency (EQE) reaches up to 90%. The J_{SC} integrated from the EQE spectrum is 31.8 mA cm^{-2}, in line with the values derived from the *J*–*V* scans. As mentioned in previous reports,[4] when the device area is larger than the optical mask used for the *J*–*V* measurements, the recorded V_{OC} values are slightly below the achievable maximum. With the optical mask removed, the V_{OC} reaches 0.90 V (**Figure S21**), ~92% of the detailed balance limit for the bandgap of this material,[60] representing one of the best results reported for PSC devices.[17, 61] The ultra-low voltage loss indicates a low rate of non-radiative charge carrier recombination in the devices.

To verify this, we compared the ideality factor of the devices by measuring the *J*–*V* curves of the cells under different light intensities. Charge carrier recombination mechanisms are reflected by the Shockley diode ideality factor (n_{id} = 1–2); when n_{id} approaches 2, Shockley-Read-Hall (SRH) type, trap-assisted recombination generally dominates, and in high V_{OC} devices n_{id} approaching 1 indicates bulk-recombination-limited cells.[62-63] As determined by the slope of the plot of V_{OC} versus incident light intensity (**Figure S22**), the ideality factor is 1.45 for the untreated and 1.41 for PP-treated devices, falling further to 1.35 for the device treated with PPCPTA, indicating a lower relative contribution from trap-mediated recombination.

We also tracked the shelf-stability of the unencapsulated mixed Sn–Pb cells stored in the dark under an N_2 atmosphere (ISOS D-1).[64] After three months (>2000 hours), the cells prepared without treatment and treated with PP retained 69% and 83% of their initial efficiencies, respectively. In contrast, the stability of the cells treated with PPCPTA was substantially improved, retaining 96% of the initial efficiency (**Figure 2f**). The evolution of the corresponding cell parameters is also given in the supporting information in **Figure S23**. We also observed positive aging effects for the cells treated with PP and PPCPTA, with the PCE of the cells treated with PPCPTA up to 22.4% after two months of storage, and V_{OC} reaching values up to 0.89 V (**Figure S23 and S24**). Based on previous reports, this might be related to the release of lattice strain and further passivation of the films after a long storage period.[65] In our particular case, we can see this aging effect already in the first week (**Figure S25**). In addition, we measured the cells stored in ambient conditions with a simple encapsulation film (**Figure S26**). The untreated, PP-treated, and PPCPTA-treated cells maintained 76%, 81%, and 90% of their initial PCE values for >450 hours, respectively. This confirms that the functionalization of perovskite interfaces enhances material and device stability significantly, and also indicates that improved encapsulation technology is necessary for PSCs to achieve lifetimes comparable to that in an inert atmosphere, a particularly acute concern for mixed Sn–Pb cells. To further improve the intrinsic robustness of this material, further strategies should be sought that can inhibit or mitigate ion migration-induced effects and simultaneously reduce the effects of chemical interaction with other layers, such as Ag from the electrode.[66-67] This could be by, for example, i) precisely inducing a well-oriented 2D perovskite component into the grain surfaces,[58] or ii) designing molecules/species with functional groups having a strong affinity towards metal centers and interacting with the halide(s) of the perovskites, while not interfering with, or ideally facilitating, charge carrier extraction.[7]

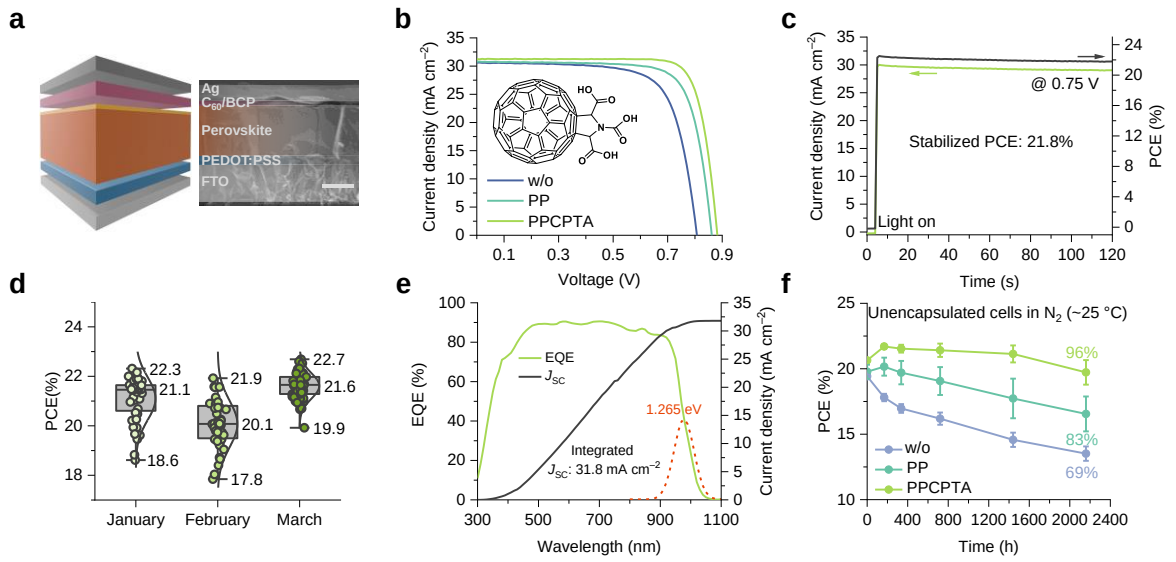

Figure 2. Cell performance. a, Schematic and cross-sectional SEM image of the device (Scale bar: 500 nm). **b,** *J*–*V* curves of the best performing mixed Sn–Pb devices (E_g = ~1.26 eV) made in the same batch. For clarity, only reverse scans are shown, more information is given in **Figure S18**. Inset shows the chemical structure of CPTA. **c,** Stabilized power output of the PPCPTA-treated device measured by fixing the voltage at 0.75 V under AM1.5 G illumination. **d,** Efficiency distribution of cells fabricated with PPCPTA treatment over three months. The champion PCE was 22.7% (**Figure S20**). **e,** EQE spectrum and integrated J_{SC} of one representative PPCPTA-treated device. –dEQE/dE (orange dashed line) is shown to estimate the bandgap of the perovskite absorber in the full device. **f,** Shelf-stability of the unencapsulated cells stored in the N_2-filled glovebox in the dark at room temperature (ISOS D-1)[64] for three months (>2000 hours).

Table 1. The photovoltaic parameters of the champion devices for untreated and treated PSCs fabricated in the same batch.

Cells	Scan[a]	J_{SC} (mA cm^{-2})	V_{OC} (V)	FF	PCE (%)
w/o	Forward	30.85	0.81	0.73	18.30
	Reverse	30.61	0.81	0.72	17.73
PP	Forward	31.12	0.87	0.79	21.37

	Reverse	30.79	0.86	0.76	20.23
PPCPTA	Forward	31.63	0.88	0.79	22.00
	Reverse	31.24	0.88	0.81	22.31

[a]Scan direction: forward and reverse denote the scan direction from J_{SC} to V_{OC} and from V_{OC} to J_{SC}, respectively.

2.3. Energy loss analysis

To determine the origin of the improved cell performance, we systematically investigated the synergistic passivation effects from the PP and PPCPTA treatments. We assessed the crystallinity of the perovskite thin films using XRD. As shown in **Figure S27**, we observed only minor changes to the XRD patterns after the treatments were applied, indicating minimal change to the bulk crystallinity of the perovskite thin films. Therefore, the improved photovoltaic performance is unlikely to be associated with enhancement of the film crystallinity, which is not unexpected due to the small amounts of material employed.[42] We then investigated the carrier dynamics using steady-state photoluminescence (PL) and time-resolved photoluminescence (TRPL) measurements, exciting the films from the top surface where we applied the modifications (details are given in supporting information). As shown in **Figure 3a**, the PL intensities of perovskite films modified with PP and PPCPTA are about 2.0 and 2.7 times higher than those of the untreated films, respectively (**Table S2**), suggesting that non-radiative recombination losses were considerably alleviated with surface passivation. We, however, also observed that the peak center shifted from 1.24 eV for the untreated films to 1.26 eV for the films treated with PP, possibly owing to lattice tilting with partial incorporation of the large PP cation at the surface.[68] It likewise provides additional evidence for the protonation of the amine at the film surface. For the films treated with PPCPTA, the spectrum indicates two components inside, one from the original untreated bulk film with a bandgap of ~1.23 eV,[37]

while the other emission at 1.28 eV is likely from the modified surface containing PP as a cation. The luminescence intensities of the two components, however, are enhanced, suggesting reduced non-radiative charge carrier recombination. This would be an interesting phenomenon to study for further understanding of perovskite surface states relating to the surface structure and carrier dynamics[69] (see **Table S2** supporting information for further discussion). From the TRPL spectra (**Figure 3b**), by fitting with a biexponential function (**Table S3**), we observed that the PP treatment slightly elongated the average carrier lifetimes of films from 4.91 μs for the untreated films to 5.27 μs, typically indicating reduced defect densities at the film surface. The addition of CPTA led to a fast-initial decay component with a carrier lifetime of 0.34 μs, which may correspond to i) carrier extraction processes since CPTA can serve as an electron acceptor; ii) an additional interface recombination pathway, as CPTA will likely assemble a layer at the perovskite surface with the carboxylate groups binding to the perovskite. The slow decay was, however, greatly extended to 8.69 μs, and thus the calculated average lifetime was 6.39 μs, which is considerably longer than that for untreated and PP-treated films. The substantially elongated charge carrier lifetimes indicate a significant suppression of surface defects, which might be A/X-site vacancies, under-coordinated metal centers, and/or Pb/Sn−I anti-sites at the film surfaces.[70]

To further verify the reduced non-radiative recombination, we conducted space-charge-limited current (SCLC) measurements that allow us to estimate the trap densities in the perovskite films (**Figure 3c**).[71] **Figure S28** shows the current−voltage (*I−V)* curves of the corresponding devices. The estimated hole trap densities for the untreated, PP-treated, and PPCPTA-treated films are 3.05×10^{15}, 2.61×10^{15}, and 2.29×10^{15} cm^{-3}, respectively. Meanwhile, the estimated electron trap densities are also greatly reduced from 1.31×10^{15} cm^{-3} for the untreated films, to 4.44×10^{14} cm^{-3} for the PP-treated, and even 3.72×10^{14} cm^{-3} for the PPCPTA-treated films. Therefore, the PPCPTA-treated films had the lowest trap-state densities for both electrons and holes.

To quantitatively evaluate the efficacy of the passivation, we conducted photoluminescence quantum yield (PLQY) measurements and quasi-Fermi level splitting (QFLS) analysis.[72-73] The experimental details are given in the supporting information. For the neat perovskite films, the PLQY values are 2.54% and 4.57% for the untreated and PP-treated ones, respectively, which is substantially increased to 6.45% for the films processed with PPCPTA, in line with the PL and TRPL results above. We also evaluated the difference in PLQY values between neat films and films covered with the electron-extracting contact (i.e., C_{60}) to examine the resulting interfacial energy losses. As shown in **Figure 3d**, the films treated with PP and PPCPTA present a significantly reduced difference in the PLQY values compared to the untreated ones, indicating a beneficial effect of the treatments on interfacial recombination. However, we also observed that the films treated with PPCPTA present a slightly increased contact loss compared to the PP-treated ones (size of grey rectangles in **Figure 3d**). This is likely caused by the additional interfacial recombination induced with the assembled CPTA layer at the surface, however, its global passivation effect is still preserved as indicated by the enhanced absolute PLQY values for both kinds of films. With the PLQY values, we can calculate the QFLS with a previously reported method.[73-74] For both the PP- and PPCPTA-treated neat perovskite films and their C_{60}-coated counterparts, the QFLS and ΔQFLS values were increased considerably compared to the untreated ones (**Figure 3e and f)**, correlating well with the V_{OC} and thus also the ΔV_{OC} values of the corresponding solar cell devices. Therefore, the large PLQY and QFLS values of the films indicate the remarkable suppression of non-radiative recombination channels in the PPCPTA-treated devices, corroborating the greatly reduced energy losses.

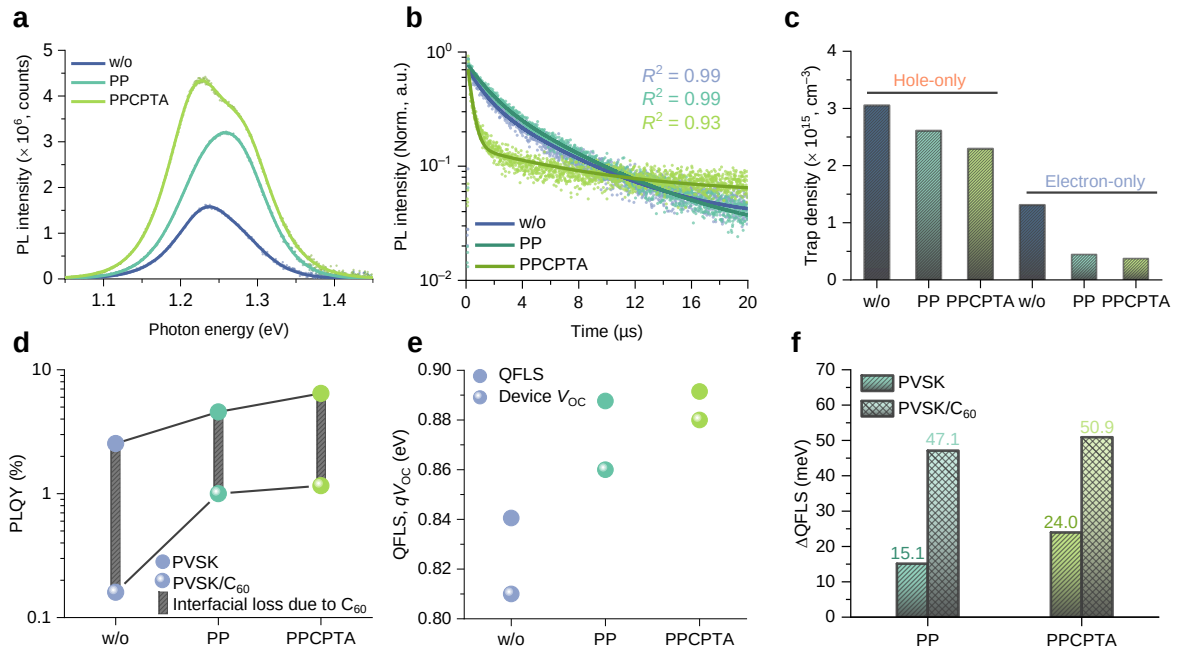

Figure 3. Energy loss analysis. a, PL spectra and **b,** TRPL decay curves of the perovskite films prepared without post-treatment, treated with PP, and PPCPTA. Films were excited from the top surface, where the post-treatments were applied. **c,** Hole and electron trap densities estimated from SCLC measurements (**Figure S28**). **d,** PLQY results for perovskite, perovskite/PP, and perovskite/PPCPTA samples, and the same sample conditions with C_{60} (20 nm) deposited on top. PVSK denotes perovskite. **e,** Comparison of the QFLS of the perovskite/treatment/C_{60} samples and the V_{OC} of the corresponding photovoltaic devices. **f**, Enhancement of the QFLS for the treated and untreated neat perovskite films and coated with C_{60}, values are given by $\Delta QFLS = 25.7 \times \ln(PLQY_{treated}/PLQY_{untreated})$ meV, which is a straightforward way to calculate the expected increase in V_{OC} for a given PLQY ratio.[72-73]

2.3. Atomic-level understanding of the defects

For a better understanding of the defect passivation at an atomic level from the view of surface chemistry,[75] we first performed X-ray photoelectron spectroscopy (XPS) characterization on the treated films. For the I peak (**Figure 4a**), a small shift by ~0.09 eV to higher binding energy can be observed by comparing the untreated sample and the samples treated with PP and

PPCPTA, while no shift is observed for the CPTA-treated films. These results indicate that, with the application of PP, the electrochemical environment of I was slightly altered, presumably owing to the enhanced electrostatic interactions induced by the incorporated PP cation at the reconstructed surface.[76] From the XPS results, we also calculated the atomic concentration of the metals at the film surface by integrating the area of the corresponding peaks. The results showed that the concentration of Sn and Pb at the film surface is 7.18% and 7.59%, respectively, suggesting that the number of octahedral units constructed with Sn^{2+} and Pb^{2+} cations is approximately the same, in line with the composition from the precursor materials. As for the Sn at the surface (**Figure 4b, S29, and Table S4**), by fitting the Sn 3*d* core level spectra, we found that the amount of Sn^{4+} decreased from 24.3% for the untreated films to 18.2% for the films processed with PP, confirming the enhanced surface quality. More importantly, when the films were treated with the solutions containing CPTA, i.e., both PPCPTA and CPTA treatments, the amount of Sn^{4+} at the film surface is greatly decreased to 7.7% and 8.3%, respectively, suggesting CPTA is capable of improving the robustness to oxidation of mixed Sn–Pb perovskite films. We then also analysed changes to the Sn chemical environments induced by the treatments. We found a slight shift of 0.12–0.16 eV towards higher binding energies for the peaks when treated with PP which is comparable for both Sn^{2+} and Sn^{4+} species. The combined PPCPTA treatment presents even stronger shifts than for PP alone. However, in this case, the influence on the shift is much more pronounced for the Sn^{4+} peaks (~0.61 eV) than for the Sn^{2+} ones (~0.34 eV). To analyse the contribution of the CPTA molecules, we studied the effect of the PP-free CPTA treatment. Interestingly, we observed the same behavior as for the PPCPTA case. The shifts are comparable to those of PPCPTA, and show an even stronger effect on the Sn^{4+} peaks (0.30–0.34 eV for Sn^{2+} and 0.59–0.68 eV for Sn^{4+}). In addition, these shifts are consistent for both Sn $3d_{3/2}$ and $3d_{5/2}$ core levels. These results indicate that while PP clearly has a positive influence on the material quality, CPTA is key to obtaining very high-quality film surfaces with both suppressed Sn^{4+} and passivated Sn-related

defects. We interpret the larger shifts for Sn^{4+} peaks with CPTA-containing treatments as CPTA establishing stronger inter-molecular interactions with higher valency Sn species. Additionally, the XPS results showed negligible peak shifts for Pb for any of the treatments (**Figure 4c**). These results indicate that, while the carboxyl groups of CPTA have a strong coordinating ability to the metal cations, CPTA has the property of selectively binding with tin rather than lead at the film surface, which is an unexpected and, to the best of our knowledge, as yet unreported phenomenon. This might be caused by the lower formation energy of iodide vacancies at the film surface within the octahedral units centered with Sn than with Pb.

We then conducted DFT calculations to evaluate the formation energy of iodide vacancies, a ubiquitous defect for perovskites,[77-78] centered with Sn^{2+} (V_I(Sn)) and Pb^{2+} (V_I(Pb)) cations (**Figure 4d, S30**). The relative formation energy of V_I(Pb) is 0.13 eV higher than that of V_I(Sn) with respect to the perfect A-I terminated (001) surface, indicating the higher energy required to break the Pb–I bond from the lattice. Therefore, at the mixed Sn–Pb film surface most of the under-coordinated metal sites will be Sn rather than Pb, resulting in the preferential passivation effect. We further modified the perovskite structure having V_I(Sn) with CPTA applied to it (**Figure 4e**). The structure is stabilized with a relative adsorption energy of –1.63 eV. The length of Sn–O bonds is 2.330 Å (**Figure 4fi**), in close alignment with the bond length in SnO_2,[79] indicating covalent bonding interactions. The electron density difference was then calculated to understand the nature of the bonding between the CPTA molecule and the perovskite surface with a V_I(Sn) defect further (**Figure 4fii**). The turquoise and yellow regions represent charge depletion and accumulation, respectively. The interaction between the electron-rich -COO^- group and the electron-poor Sn^{2+} cation results in two strong Sn–O bonds. Meanwhile, the other two -COO^- groups may interact with the surrounding A-site cations as well, reducing the possibility of forming defects, such as A-site vacancies, at the surface. At the same time, we also investigated the possible passivation effects from the applied PP molecule. As we conclude above, PP will be protonated to the corresponding cation via the reaction with the organic

cation(s) at the perovskite film surface. Thus, we mainly considered the passivation of the A-site vacancies at the surface by PP^{2+} cations. From the results, we found that perovskite films with vacancies of Cs^+ (V_{Cs}), FA^+ (V_{FA}), and MA^+ (V_{MA}) are stabilized with relative adsorption energies of –0.66, –0.75, and –0.41 eV, respectively, after modulation with the PP^{2+} cation at the corresponding vacancies (**Figure S31**), indicating stabilization of the surface structure. With the atomic-level understanding of the surface defects, we propose a mechanism for the synergistic surface modification of the mixed Sn–Pb perovskite films in **Figure 4g**.

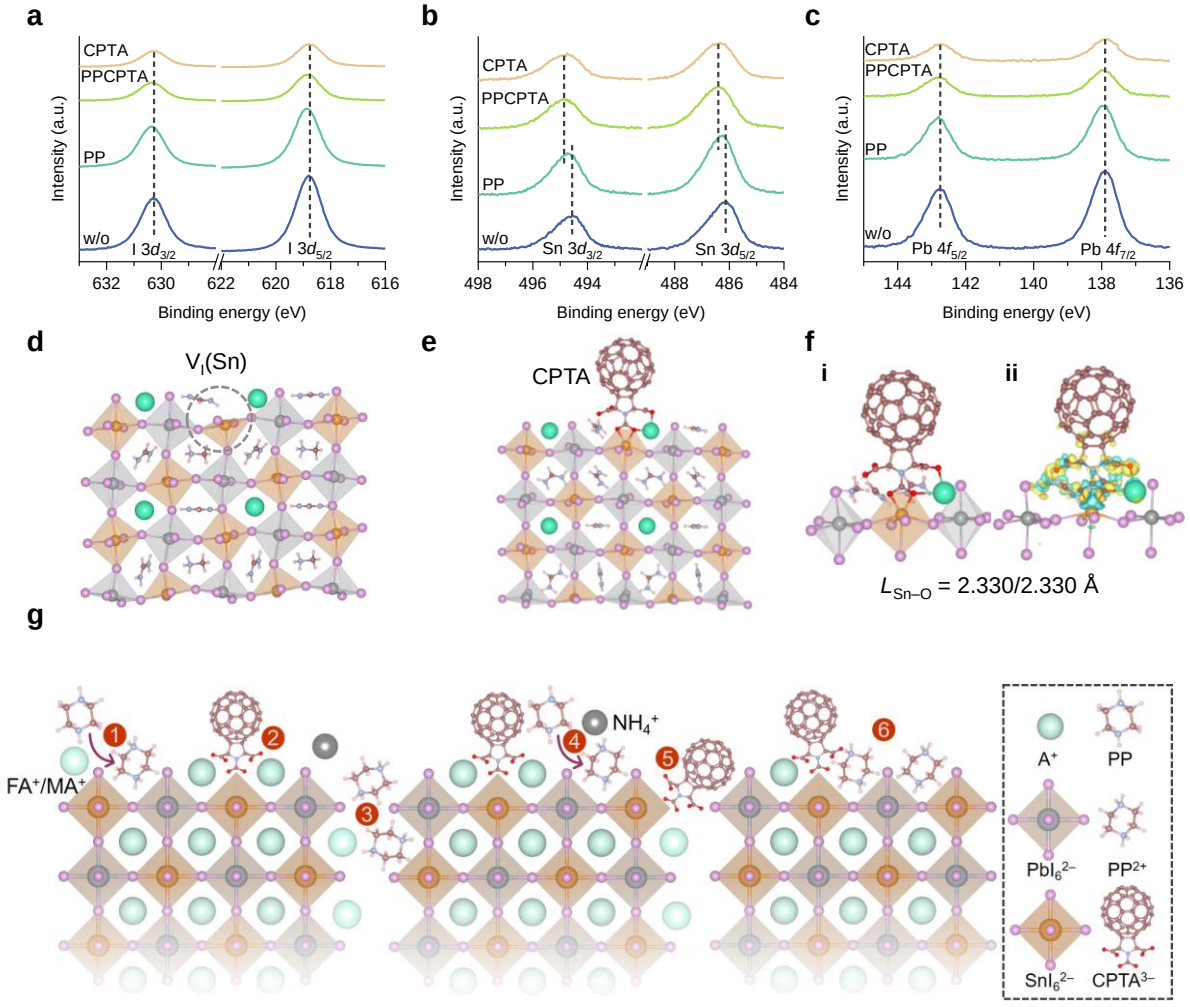

Figure 4. Atomic-level understandings. XPS spectra of the perovskite films prepared without post-treatment, treated with PP, PPCPTA, and CPTA for **a,** I $3d_{3/2}$ and $3d_{5/2}$, **b,** Sn $3d_{3/2}$ and $3d_{5/2}$, and **c,** Pb $4f_{5/2}$ and $4f_{7/2}$ core levels. For the spectra here, the signal background of each component was subtracted using the Shirley method. Additional information is given in **Figure**

S29 and Table S4. d, A-I terminated (001) surface with V_I(Sn). Only the single layer with the I vacancy is shown for clarity. Additional information is given in **Figure S30. e,** Adsorption configuration of CPTA at the perovskite surface with V_I(Sn) and the resultant binding energy is –1.63 eV. **f,** i) Expanded view of adsorption configuration of CPTA at the perovskite surface with the Sn–O bond length of 2.330 Å. ii) Electron density difference map for the CPTA molecule when bound to the perovskite surface with V_I(Sn). Pb, grey; Sn, orange; Cs, green; N, blue; I, pink; O, red; C, brown; H, light pink. **g,** Scheme of the proposed mechanism for the synergistic surface modification of the mixed Sn–Pb perovskite films. 1) Proton transfer from FA^+/MA^+ to PP, 2) CPTA binding to Sn^{2+}, 3) PP cations penetrating into grain boundaries, 4) proton transfer from NH_4^+ to PP, 5) CPTA binding to Sn^{2+} at the grain boundaries, 6) PP cations settling at the adjacent A-site vacancies, and H-bonding interactions between CPTA and PP cations.

3. Conclusion

In summary, we have developed a robust, synergistic surface post-treatment for narrow bandgap, mixed Sn–Pb perovskites for solar cells with state-of-the-art performance. Firstly, we unveiled the role shared between the amine and ammonium post-treatment of perovskite films. We found that when applied at the surface of films, the amines studied here will react with the organic cation(s) in the perovskite films. Thus, amines are protonated to their conjugate ammonium, which will reconstruct the perovskite component *in situ* by binding to the A-site, or in some cases even by forming low dimensional phases at the surface. These treated surfaces are energetically more favorable for electron extraction at the interface with C_{60}. Meanwhile, the application of the fullerene derivative CPTA together with PP led to negligible hysteresis and excellent performance of solar cells with PCE values up to 22.7% and V_{OC} values approaching 0.90 V, representing one of the best cells reported with the bandgap ~1.26 eV. Importantly, the

functionalization of the interface with the PPCPTA delivered greatly enhanced stability. Unencapsulated cells presented 96% efficiency retention after >2000 hours of storage in an N_2-filled glovebox and encapsulated cells retained 90% of their initial efficiency after >450 hours of storage in ambient conditions. This is likely due to the mitigation of ion migration effects, passivated defect states, and reduced interaction with impurities from the top layers. In addition, we found that the functionalized fullerene, CPTA, preferentially interacts with Sn centers rather than Pb at the film surface. Further theoretical investigations revealed that iodide vacancies formed at the octahedral units centered with Sn are energetically more favored than with Pb. Therefore, the under-coordinated metal sites at mixed Sn–Pb perovskite film surfaces will mostly be Sn centers, verifying the intriguing selective passivation. This finding may explain the particularly beneficial nature of surface engineering for Sn-containing perovskite materials. Assisted with further complementary surface science or spectroscopic techniques, an even richer picture could emerge of the phenomena arising from the specific defects at the complex perovskite surface. Overall, this work not only provides a simple post-treatment method for achieving efficient and stable inverted PSCs, but also delivers a comprehensive atomic understanding of the specific defect passivation required for mixed Sn–Pb perovskites, highlighting the critical importance of interfaces for further improving the performance of perovskite optoelectronics.

Supporting Information

Supporting Information is available from the Wiley Online Library or from the author.

Author contributions

S. H. conceived the idea. S. H. measured the SEM. R. M. performed AFM characterization. S. H. conducted the XRD and 2D GIWAXS measurement with the help of N. S. and T. H., and analysed the results with the help of J. A. S. and H. J. S.; S. H. prepared the single crystal and

refined the structure. S. H. carried out the PL measurements with the help of T. Y. and Y. K.; S. H. fabricated the solar cell devices and performed the related characterizations. S. H. conducted the optical absorption measurement with the help of M. A. T.; K. N. and K. T. conducted the UPS and XPS measurements. S. H. conducted the SCLC measurements. S. H. and J. P. conducted the NMR characterizations. R. D. J. O. and J. A. S. performed the PLQY and QFLS characterizations under the supervision of M. B. J. and H. J. S.; P. Z. and M. E. conducted the DFT calculations. S. H., J. P., J. A. S., and R. D. J. O. prepared the manuscript. H. J. S. and A. W. supervised the project. All authors commented on the manuscript.

Conflicts of interest

H. J. S. is co-founder and CSO of Oxford PV Ltd.

A. W. is co-founder and CSO of Enecoat Technologies Co., Ltd.

Acknowledgments

This work was partially supported by JST–ALCA (JPMJAL1603) and JST–COI (JPMJCE1307) programs, NEDO, JST-Mirai Program (JPMJMI22E2), International Collaborative Research Program of ICR, Kyoto University, ICR Grants for Promoting Integrated Research, Kyoto University, grants for the Integrated Research Consortium on Chemical Sciences, Grant-in-Aid for Research Activity Start-up (20K22531), Grant-in-Aid for Early-Career Scientists (JP22K14744), Grant-in-Aid for Scientific Research (C) (19K05666) and Grant-in-Aid for Scientific Research (A) (21H04699), JSPS for a Research Fellowship for Young Scientists (21J14762), and the China Scholarship Council (CSC). M. E. thanks the financial support from JSPS KAKENHI (JP20H02718). The computations were partly performed using Research Centre for Computational Science, Okazaki, Japan (Project: 22-IMS-C185). R. D. J. O would like to express his gratitude to the Penrose Scholarship for Funding his studentship. We thank Tao Fang (Kyoto University) for assistance with XRD measurements,

Yasuko Iwasaki (Kyoto University) for assistance with SEM measurements, Tiancheng Tan (Kyoto University) for assistance with NMR measurements, Dr Yoshiyuki Mizuhata and Prof. Norihiro Tokitoh (Kyoto University) for assistance with single crystal XRD measurements, Ajinomoto FineTechno Co., Inc. for providing the encapsulation materials.

Received: ((will be filled in by the editorial staff))
Revised: ((will be filled in by the editorial staff))
Published online: ((will be filled in by the editorial staff))

References

1. Green, M. A.; Ho-Baillie, A.; Snaith, H. J., The emergence of perovskite solar cells. *Nat. Photonics* **2014**, *8*, 506–514.

2. Stranks, S. D.; Snaith, H. J., Metal-halide perovskites for photovoltaic and light-emitting devices. *Nat. Nanotechnol.* **2015**, *10*, 391–402.

3. Huang, J.; Yuan, Y.; Shao, Y.; Yan, Y., Understanding the physical properties of hybrid perovskites for photovoltaic applications. *Nat. Rev. Mater.* **2017**, *2*, 17042.

4. Yoo, J. J.; Seo, G.; Chua, M. R.; Park, T. G.; Lu, Y.; Rotermund, F.; Kim, Y.-K.; Moon, C. S.; Jeon, N. J.; Correa-Baena, J.-P.; Bulović, V.; Shin, S. S.; Bawendi, M. G.; Seo, J., Efficient perovskite solar cells via improved carrier management. *Nature* **2021**, *590*, 587–593.

5. Kim, M.; Jeong, J.; Lu, H.; Lee Tae, K.; Eickemeyer Felix, T.; Liu, Y.; Choi In, W.; Choi Seung, J.; Jo, Y.; Kim, H.-B.; Mo, S.-I.; Kim, Y.-K.; Lee, H.; An Na, G.; Cho, S.; Tress Wolfgang, R.; Zakeeruddin Shaik, M.; Hagfeldt, A.; Kim Jin, Y.; Grätzel, M.; Kim Dong, S., Conformal quantum dot–SnO_2 layers as electron transporters for efficient perovskite solar cells. *Science* **2022**, *375*, 302–306.

6. Kim, J. Y.; Lee, J.-W.; Jung, H. S.; Shin, H.; Park, N.-G., High-efficiency perovskite solar cells. *Chem. Rev.* **2020**, *120*, 7867–7918.

7. Li, Z.; Li, B.; Wu, X.; Sheppard Stephanie, A.; Zhang, S.; Gao, D.; Long Nicholas, J.; Zhu, Z., Organometallic-functionalized interfaces for highly efficient inverted perovskite solar cells. *Science* **2022**, *376*, 416–420.

8. Jiang, Q.; Tong, J.; Xian, Y.; Kerner, R. A.; Dunfield, S. P.; Xiao, C.; Scheidt, R. A.; Kuciauskas, D.; Wang, X.; Hautzinger, M. P.; Tirawat, R.; Beard, M. C.; Fenning, D. P.; Berry, J. J.; Larson, B. W.; Yan, Y.; Zhu, K., Surface reaction for efficient and stable inverted perovskite solar cells. *Nature* **2022**, *https://doi.org/10.1038/s41586-022-05268-x*.

9. Green, M. A.; Dunlop, E. D.; Hohl-Ebinger, J.; Yoshita, M.; Kopidakis, N.; Bothe, K.; Hinken, D.; Rauer, M.; Hao, X., Solar cell efficiency tables (Version 60). *Prog. Photovolt.: Res. Appl.* **2022**, *30*, 687–701.

10. Xue, J.; Wang, R.; Yang, Y., The surface of halide perovskites from nano to bulk. *Nat. Rev. Mater.* **2020**, *5*, 809–827.

11. Luo, D.; Su, R.; Zhang, W.; Gong, Q.; Zhu, R., Minimizing non-radiative recombination losses in perovskite solar cells. *Nat. Rev. Mater.* **2020**, *5*, 44–60.

12. Kroemer, H., Nobel Lecture: quasielectric fields and band offsets: teaching electrons new tricks. *Rev. Mod. Phys.* **2001**, *73*, 783–793.

13. Zheng, X.; Chen, B.; Dai, J.; Fang, Y.; Bai, Y.; Lin, Y.; Wei, H.; Zeng, X.; Huang, J., Defect passivation in hybrid perovskite solar cells using quaternary ammonium halide anions and cations. *Nat. Energy* **2017**, *2*, 17102.

14. Zheng, X.; Hou, Y.; Bao, C.; Yin, J.; Yuan, F.; Huang, Z.; Song, K.; Liu, J.; Troughton, J.; Gasparini, N.; Zhou, C.; Lin, Y.; Xue, D.-J.; Chen, B.; Johnston, A. K.; Wei, N.; Hedhili, M. N.; Wei, M.; Alsalloum, A. Y.; Maity, P.; Turedi, B.; Yang, C.; Baran, D.; Anthopoulos, T. D.; Han, Y.; Lu, Z.-H.; Mohammed, O. F.; Gao, F.; Sargent, E. H.; Bakr, O. M., Managing grains and interfaces via ligand anchoring enables 22.3%-efficiency inverted perovskite solar cells. *Nat. Energy* **2020**, *5*, 131–140.

15. Stolterfoht, M.; Wolff, C. M.; Márquez, J. A.; Zhang, S.; Hages, C. J.; Rothhardt, D.; Albrecht, S.; Burn, P. L.; Meredith, P.; Unold, T.; Neher, D., Visualization and suppression of interfacial recombination for high-efficiency large-area pin perovskite solar cells. *Nat. Energy* **2018**, *3*, 847–854.

16. Li, F.; Deng, X.; Qi, F.; Li, Z.; Liu, D.; Shen, D.; Qin, M.; Wu, S.; Lin, F.; Jang, S.-H.; Zhang, J.; Lu, X.; Lei, D.; Lee, C.-S.; Zhu, Z.; Jen, A. K. Y., Regulating surface termination for efficient inverted perovskite solar cells with greater than 23% efficiency. *J. Am. Chem. Soc.* **2020**, *142*, 20134–20142.

17. Li, X.; Zhang, W.; Guo, X.; Lu, C.; Wei, J.; Fang, J., Constructing heterojunctions by surface sulfidation for efficient inverted perovskite solar cells. *Science* **2022**, *375*, 434–437.

18. Azmi, R.; Ugur, E.; Seitkhan, A.; Aljamaan, F.; Subbiah Anand, S.; Liu, J.; Harrison George, T.; Nugraha Mohamad, I.; Eswaran Mathan, K.; Babics, M.; Chen, Y.; Xu, F.; Allen Thomas, G.; Rehman Atteq, u.; Wang, C.-L.; Anthopoulos Thomas, D.; Schwingenschlögl, U.; De Bastiani, M.; Aydin, E.; De Wolf, S., Damp heat–stable perovskite solar cells with tailored-dimensionality 2D/3D heterojunctions. *Science* **2022**, *376*, 73–77.

19. Klug, M. T.; Milot, R. L.; Patel, J. B.; Green, T.; Sansom, H. C.; Farrar, M. D.; Ramadan, A. J.; Martani, S.; Wang, Z.; Wenger, B.; Ball, J. M.; Langshaw, L.; Petrozza, A.; Johnston,

M. B.; Herz, L. M.; Snaith, H. J., Metal composition influences optoelectronic quality in mixed-metal lead–tin triiodide perovskite solar absorbers. *Energy Environ. Sci.* **2020**, *13*, 1776–1787.

20. Goyal, A.; McKechnie, S.; Pashov, D.; Tumas, W.; van Schilfgaarde, M.; Stevanović, V., Origin of pronounced nonlinear band gap behavior in lead–tin hybrid perovskite alloys. *Chem. Mater.* **2018**, *30*, 3920–3928.

21. Lin, R.; Xu, J.; Wei, M.; Wang, Y.; Qin, Z.; Liu, Z.; Wu, J.; Xiao, K.; Chen, B.; Park, S. M.; Chen, G.; Atapattu, H. R.; Graham, K. R.; Xu, J.; Zhu, J.; Li, L.; Zhang, C.; Sargent, E. H.; Tan, H., All-perovskite tandem solar cells with improved grain surface passivation. *Nature* **2022**, *603*, 73–78.

22. Wang, C.; Song, Z.; Li, C.; Zhao, D.; Yan, Y., Low-bandgap mixed tin–lead perovskites and their applications in all-perovskite tandem solar cells. *Adv. Funct. Mater.* **2019**, *29*, 1808801.

23. Shockley, W.; Queisser, H. J., Detailed balance limit of efficiency of p–n junction solar cells. *J. Appl. Phys.* **1961**, *32*, 510–519.

24. Li, Z.; Zhao, Y.; Wang, X.; Sun, Y.; Zhao, Z.; Li, Y.; Zhou, H.; Chen, Q., Cost analysis of perovskite tandem photovoltaics. *Joule* **2018**, *2*, 1559–1572.

25. Gu, S.; Lin, R.; Han, Q.; Gao, Y.; Tan, H.; Zhu, J., Tin and mixed lead–tin halide perovskite solar cells: progress and their application in tandem solar cells. *Adv. Mater.* **2020**, *32*, 1907392.

26. Rajagopal, A.; Liang, P.-W.; Chueh, C.-C.; Yang, Z.; Jen, A. K. Y., Defect passivation via a graded fullerene heterojunction in low-bandgap Pb–Sn binary perovskite photovoltaics. *ACS Energy Lett.* **2017**, *2*, 2531–2539.

27. Saidaminov, M. I.; Spanopoulos, I.; Abed, J.; Ke, W.; Wicks, J.; Kanatzidis, M. G.; Sargent, E. H., Conventional solvent oxidizes Sn(II) in perovskite inks. *ACS Energy Lett.* **2020**, *5*, 1153–1155.

28. Pascual, J.; Di Girolamo, D.; Flatken, M. A.; Aldamasy, M. H.; Li, G.; Li, M.; Abate, A., Lights and shadows of DMSO as solvent for tin halide perovskites. *Chem. Eur. J.* **2022**, *28*, e202103919.

29. Hu, S.; Truong, M. A.; Otsuka, K.; Handa, T.; Yamada, T.; Nishikubo, R.; Iwasaki, Y.; Saeki, A.; Murdey, R.; Kanemitsu, Y.; Wakamiya, A., Mixed lead–tin perovskite films with >7 μs charge carrier lifetimes realized by maltol post-treatment. *Chem. Sci.* **2021**, *12*, 13513–13519.

30. Dong, H.; Ran, C.; Gao, W.; Sun, N.; Liu, X.; Xia, Y.; Chen, Y.; Huang, W., Crystallization dynamics of Sn-based perovskite thin films: Toward efficient and stable photovoltaic devices. *Adv. Energy Mater.* **2022**, *12*, 2102213.

31. Liu, H.; Wang, L.; Li, R.; Shi, B.; Wang, P.; Zhao, Y.; Zhang, X., Modulated crystallization and reduced V_{OC} deficit of mixed lead–tin perovskite solar cells with antioxidant caffeic acid. *ACS Energy Lett.* **2021**, *6*, 2907–2916.

32. Wei, M.; Xiao, K.; Walters, G.; Lin, R.; Zhao, Y.; Saidaminov, M. I.; Todorović, P.; Johnston, A.; Huang, Z.; Chen, H.; Li, A.; Zhu, J.; Yang, Z.; Wang, Y.-K.; Proppe, A. H.; Kelley, S. O.; Hou, Y.; Voznyy, O.; Tan, H.; Sargent, E. H., Combining efficiency and stability in mixed tin–lead perovskite solar cells by capping grains with an ultrathin 2D layer. *Adv. Mater.* **2020**, *32*, 1907058.

33. Chen, H.; Teale, S.; Chen, B.; Hou, Y.; Grater, L.; Zhu, T.; Bertens, K.; Park, S. M.; Atapattu, H. R.; Gao, Y.; Wei, M.; Johnston, A. K.; Zhou, Q.; Xu, K.; Yu, D.; Han, C.; Cui,

T.; Jung, E. H.; Zhou, C.; Zhou, W.; Proppe, A. H.; Hoogland, S.; Laquai, F.; Filleter, T.; Graham, K. R.; Ning, Z.; Sargent, E. H., Quantum-size-tuned heterostructures enable efficient and stable inverted perovskite solar cells. *Nat. Photonics* **2022**, *16*, 352–358.

34. Hu, M.; Chen, M.; Guo, P.; Zhou, H.; Deng, J.; Yao, Y.; Jiang, Y.; Gong, J.; Dai, Z.; Zhou, Y.; Qian, F.; Chong, X.; Feng, J.; Schaller, R. D.; Zhu, K.; Padture, N. P.; Zhou, Y., Sub-1.4eV bandgap inorganic perovskite solar cells with long-term stability. *Nat. Commun.* **2020**, *11*, 151.

35. Zeng, L.; Chen, Z.; Qiu, S.; Hu, J.; Li, C.; Liu, X.; Liang, G.; Brabec, C. J.; Mai, Y.; Guo, F., 2D-3D heterostructure enables scalable coating of efficient low-bandgap Sn–Pb mixed perovskite solar cells. *Nano Energy* **2019**, *66*, 104099.

36. Kapil, G.; Bessho, T.; Maekawa, T.; Baranwal, A. K.; Zhang, Y.; Kamarudin, M. A.; Hirotani, D.; Shen, Q.; Segawa, H.; Hayase, S., Tin-lead perovskite fabricated via ethylenediamine interlayer guides to the solar cell efficiency of 21.74%. *Adv. Energy Mater.* **2021**, *11*, 2101069.

37. Hu, S.; Otsuka, K.; Murdey, R.; Nakamura, T.; Truong, M. A.; Yamada, T.; Handa, T.; Matsuda, K.; Nakano, K.; Sato, A.; Marumoto, K.; Tajima, K.; Kanemitsu, Y.; Wakamiya, A., Optimized carrier extraction at interfaces for 23.6% efficient tin–lead perovskite solar cells. *Energy Environ. Sci.* **2022**, *15*, 2096–2107.

38. Dessimoz, M.; Yoo, S.-M.; Kanda, H.; Igci, C.; Kim, H.; Nazeeruddin, M. K., Phase-pure quasi-2D perovskite by protonation of neutral amine. *J. Phys. Chem. Lett.* **2021**, *12*, 11323–11329.

39. Mao, L.; Ke, W.; Pedesseau, L.; Wu, Y.; Katan, C.; Even, J.; Wasielewski, M. R.; Stoumpos, C. C.; Kanatzidis, M. G., Hybrid Dion–Jacobson 2D lead iodide perovskites. *J. Am. Chem. Soc.* **2018**, *140*, 3775–3783.

40. Noel, N. K.; Wenger, B.; Habisreutinger, S. N.; Snaith, H. J., Utilizing nonpolar organic solvents for the deposition of metal-halide perovskite films and the realization of organic semiconductor/perovskite composite photovoltaics. *ACS Energy Lett.* **2022**, *7*, 1246–1254.

41. Kim, H.; Kim, J. S.; Heo, J.-M.; Pei, M.; Park, I.-H.; Liu, Z.; Yun, H. J.; Park, M.-H.; Jeong, S.-H.; Kim, Y.-H.; Park, J.-W.; Oveisi, E.; Nagane, S.; Sadhanala, A.; Zhang, L.; Kweon, J. J.; Lee, S. K.; Yang, H.; Jang, H. M.; Friend, R. H.; Loh, K. P.; Nazeeruddin, M. K.; Park, N.-G.; Lee, T.-W., Proton-transfer-induced 3D/2D hybrid perovskites suppress ion migration and reduce luminance overshoot. *Nat. Commun.* **2020**, *11*, 3378.

42. Ansari, F.; Shirzadi, E.; Salavati-Niasari, M.; LaGrange, T.; Nonomura, K.; Yum, J.-H.; Sivula, K.; Zakeeruddin, S. M.; Nazeeruddin, M. K.; Grätzel, M.; Dyson, P. J.; Hagfeldt, A., Passivation mechanism exploiting surface dipoles affords high-performance perovskite solar cells. *J. Am. Chem. Soc.* **2020**, *142*, 11428–11433.

43. Brinkmann, K. O.; Becker, T.; Zimmermann, F.; Kreusel, C.; Gahlmann, T.; Theisen, M.; Haeger, T.; Olthof, S.; Tückmantel, C.; Günster, M.; Maschwitz, T.; Göbelsmann, F.; Koch, C.; Hertel, D.; Caprioglio, P.; Peña-Camargo, F.; Perdigón-Toro, L.; Al-Ashouri, A.; Merten, L.; Hinderhofer, A.; Gomell, L.; Zhang, S.; Schreiber, F.; Albrecht, S.; Meerholz, K.; Neher, D.; Stolterfoht, M.; Riedl, T., Perovskite–organic tandem solar cells with indium oxide interconnect. *Nature* **2022**, *604*, 280–286.

44. Chen, B.; Yang, M.; Priya, S.; Zhu, K., Origin of *J–V* hysteresis in perovskite solar cells. *J. Phys. Chem. Lett.* **2016**, *7*, 905–917.

45. Fang, Y.; Bi, C.; Wang, D.; Huang, J., The functions of fullerenes in hybrid perovskite solar cells. *ACS Energy Lett.* **2017**, *2*, 782–794.

46. Castro, E.; Murillo, J.; Fernandez-Delgado, O.; Echegoyen, L., Progress in fullerene-based hybrid perovskite solar cells. *J. Mater. Chem. C* **2018**, *6*, 2635–2651.

47. Tumen-Ulzii, G.; Matsushima, T.; Klotz, D.; Leyden, M. R.; Wang, P.; Qin, C.; Lee, J.-W.; Lee, S.-J.; Yang, Y.; Adachi, C., Hysteresis-less and stable perovskite solar cells with a self-assembled monolayer. *Commun. Mater.* **2020**, *1*, 31.

48. Jia, L.; Huang, F.; Ding, H.; Niu, C.; Shang, Y.; Hu, W.; Li, X.; Yu, X.; Jiang, X.; Cao, R.; Zhu, J.; Wang, G.-W.; Chen, M.; Yang, S., Double-site defect passivation of perovskite film via fullerene additive engineering toward highly efficient and stable bulk heterojunction solar cells. *Nano Today* **2021**, *39*, 101164.

49. Xing, Z.; Li, S. H.; Yang, S. H., Targeted molecular design of functionalized fullerenes for high-performance and stable perovskite solar cells. *Small Struct.* **2022**, *3*, 2200012.

50. Yuan, Y.; Huang, J., Ion migration in organometal trihalide perovskite and its impact on photovoltaic efficiency and stability. *Acc. Chem. Res.* **2016**, *49*, 286–293.

51. Tress, W.; Correa Baena, J. P.; Saliba, M.; Abate, A.; Graetzel, M., Inverted current–voltage hysteresis in mixed perovskite solar cells: polarization, energy barriers, and defect recombination. *Adv. Energy Mater.* **2016**, *6*, 1600396.

52. Kang, D.-H.; Park, N.-G., On the current–voltage hysteresis in perovskite solar cells: dependence on perovskite composition and methods to remove hysteresis. *Adv. Mater.* **2019**, *31*, 1805214.

53. Lin, X.; Cui, D.; Luo, X.; Zhang, C.; Han, Q.; Wang, Y.; Han, L., Efficiency progress of inverted perovskite solar cells. *Energy Environ. Sci.* **2020**, *13*, 3823–3847.

54. Kapil, G.; Bessho, T.; Sanehira, Y.; Sahamir, S. R.; Chen, M.; Baranwal, A. K.; Liu, D.; Sono, Y.; Hirotani, D.; Nomura, D.; Nishimura, K.; Kamarudin, M. A.; Shen, Q.; Segawa, H.; Hayase, S., Tin–lead perovskite solar cells fabricated on hole selective monolayers. *ACS Energy Lett.* **2022**, *7*, 966–974.

55. Yu, D.; Wei, Q.; Li, H.; Xie, J.; Jiang, X.; Pan, T.; Wang, H.; Pan, M.; Zhou, W.; Liu, W.; Chow, P. C. Y.; Ning, Z., Quasi-2D bilayer surface passivation for high efficiency narrow bandgap perovskite solar cells. *Angew Chem Int Ed* **2022**, *61*, e202202346.

56. Cao, J.; Loi, H.-L.; Xu, Y.; Guo, X.; Wang, N.; Liu, C.-k.; Wang, T.; Cheng, H.; Zhu, Y.; Li, M. G.; Wong, W.-Y.; Yan, F., High-performance tin–lead mixed-perovskite solar cells with vertical compositional gradient. *Adv. Mater.* **2022**, *34*, 2107729.

57. Peng, C.; Li, C.; Zhu, M.; Zhang, C.; Jiang, X.; Yin, H.; He, B.; Li, H.; Li, M.; So, S. K.; Zhou, Z., Reducing energy disorder for efficient and stable Sn−Pb alloyed perovskite solar cells. *Angew Chem Int Ed* **2022**, *n/a*, e202201209.

58. Tong, J.; Jiang, Q.; Ferguson, A. J.; Palmstrom, A. F.; Wang, X.; Hao, J.; Dunfield, S. P.; Louks, A. E.; Harvey, S. P.; Li, C.; Lu, H.; France, R. M.; Johnson, S. A.; Zhang, F.; Yang, M.; Geisz, J. F.; McGehee, M. D.; Beard, M. C.; Yan, Y.; Kuciauskas, D.; Berry, J. J.; Zhu, K., Carrier control in Sn–Pb perovskites via 2D cation engineering for all-perovskite tandem solar cells with improved efficiency and stability. *Nat. Energy* **2022**, *7*, 642–651.

59. Wang, C.; Zhao, Y.; Ma, T.; An, Y.; He, R.; Zhu, J.; Chen, C.; Ren, S.; Fu, F.; Zhao, D.; Li, X., A universal close-space annealing strategy towards high-quality perovskite absorbers enabling efficient all-perovskite tandem solar cells. *Nat. Energy* **2022**, *7*, 744–753.

60. Rühle, S., Tabulated values of the Shockley–Queisser limit for single junction solar cells. *Sol. Energy* **2016**, *130*, 139–147.

61. Jeong, M.; Choi, I. W.; Go, E. M.; Cho, Y.; Kim, M.; Lee, B.; Jeong, S.; Jo, Y.; Choi, H. W.; Lee, J.; Bae, J.-H.; Kwak, S. K.; Kim, D. S.; Yang, C., Stable perovskite solar cells with efficiency exceeding 24.8% and 0.3-V voltage loss. *Science* **2020**, *369*, 1615.

62. Caprioglio, P.; Wolff, C. M.; Sandberg, O. J.; Armin, A.; Rech, B.; Albrecht, S.; Neher, D.; Stolterfoht, M., On the origin of the ideality factor in perovskite solar cells. *Adv. Energy Mater.* **2020**, *10*, 2000502.

63. Sherkar, T. S.; Momblona, C.; Gil-Escrig, L.; Ávila, J.; Sessolo, M.; Bolink, H. J.; Koster, L. J. A., Recombination in perovskite solar cells: significance of grain boundaries, interface traps, and defect ions. *ACS Energy Lett.* **2017**, *2*, 1214–1222.

64. Khenkin, M. V.; Katz, E. A.; Abate, A.; Bardizza, G.; Berry, J. J.; Brabec, C.; Brunetti, F.; Bulović, V.; Burlingame, Q.; Di Carlo, A.; Cheacharoen, R.; Cheng, Y.-B.; Colsmann, A.; Cros, S.; Domanski, K.; Dusza, M.; Fell, C. J.; Forrest, S. R.; Galagan, Y.; Di Girolamo, D.; Grätzel, M.; Hagfeldt, A.; von Hauff, E.; Hoppe, H.; Kettle, J.; Köbler, H.; Leite, M. S.; Liu, S.; Loo, Y.-L.; Luther, J. M.; Ma, C.-Q.; Madsen, M.; Manceau, M.; Matheron, M.; McGehee, M.; Meitzner, R.; Nazeeruddin, M. K.; Nogueira, A. F.; Odabaşı, Ç.; Osherov, A.; Park, N.-G.; Reese, M. O.; De Rossi, F.; Saliba, M.; Schubert, U. S.; Snaith, H. J.; Stranks, S. D.; Tress, W.; Troshin, P. A.; Turkovic, V.; Veenstra, S.; Visoly-Fisher, I.; Walsh, A.; Watson, T.; Xie, H.; Yıldırım, R.; Zakeeruddin, S. M.; Zhu, K.; Lira-Cantu, M., Consensus statement for stability assessment and reporting for perovskite photovoltaics based on ISOS procedures. *Nat. Energy* **2020**, *5*, 35–49.

65. Jokar, E.; Chien, C.-H.; Fathi, A.; Rameez, M.; Chang, Y.-H.; Diau, E. W.-G., Slow surface passivation and crystal relaxation with additives to improve device performance and durability for tin-based perovskite solar cells. *Energy Environ. Sci.* **2018**, *11*, 2353–2362.

66. Kato, Y.; Ono, L. K.; Lee, M. V.; Wang, S.; Raga, S. R.; Qi, Y., Silver iodide formation in methyl ammonium lead iodide perovskite solar cells with silver top electrodes. *Adv. Mater. Interfaces* **2015**, *2*, 1500195.

67. Li, J.; Dong, Q.; Li, N.; Wang, L., Direct evidence of ion diffusion for the silver-electrode-induced thermal degradation of inverted perovskite solar cells. *Adv. Energy Mater.* **2017**, *7*, 1602922.

68. Amat, A.; Mosconi, E.; Ronca, E.; Quarti, C.; Umari, P.; Nazeeruddin, M. K.; Grätzel, M.; De Angelis, F., Cation-induced band-gap tuning in organohalide perovskites: interplay of spin–orbit coupling and octahedra tilting. *Nano Lett.* **2014**, *14*, 3608–3616.

69. Frohna, K.; Anaya, M.; Macpherson, S.; Sung, J.; Doherty, T. A. S.; Chiang, Y.-H.; Winchester, A. J.; Orr, K. W. P.; Parker, J. E.; Quinn, P. D.; Dani, K. M.; Rao, A.; Stranks, S. D., Nanoscale chemical heterogeneity dominates the optoelectronic response of alloyed perovskite solar cells. *Nat. Nanotechnol.* **2022**, *17*, 190–196.

70. Ball, J. M.; Petrozza, A., Defects in perovskite-halides and their effects in solar cells. *Nat. Energy* **2016**, *1*, 16149.

71. Zhang, Y.; Wang, P.; Tang, M.-C.; Barrit, D.; Ke, W.; Liu, J.; Luo, T.; Liu, Y.; Niu, T.; Smilgies, D.-M.; Yang, Z.; Liu, Z.; Jin, S.; Kanatzidis, M. G.; Amassian, A.; Liu, S. F.; Zhao, K., Dynamical transformation of two-dimensional perovskites with alternating cations in the interlayer space for high-performance photovoltaics. *J. Am. Chem. Soc.* **2019**, *141*, 2684–2694.

72. Oliver, R. D. J.; Lin, Y.-H.; Horn, A. J.; Xia, C. Q.; Warby, J. H.; Johnston, M. B.; Ramadan, A. J.; Snaith, H. J., Thermally stable passivation toward high efficiency inverted perovskite solar cells. *ACS Energy Lett.* **2020**, *5*, 3336–3343.

73. Caprioglio, P.; Stolterfoht, M.; Wolff, C. M.; Unold, T.; Rech, B.; Albrecht, S.; Neher, D., On the relation between the open-circuit voltage and quasi-Fermi level splitting in efficient perovskite solar cells. *Adv. Energy Mater.* **2019**, *9*, 1901631.

74. Oliver, R. D. J.; Caprioglio, P.; Peña-Camargo, F.; Buizza, L. R. V.; Zu, F.; Ramadan, A. J.; Motti, S. G.; Mahesh, S.; McCarthy, M. M.; Warby, J. H.; Lin, Y.-H.; Koch, N.; Albrecht, S.; Herz, L. M.; Johnston, M. B.; Neher, D.; Stolterfoht, M.; Snaith, H. J., Understanding and suppressing non-radiative losses in methylammonium-free wide-bandgap perovskite solar cells. *Energy Environ. Sci.* **2022**, *15*, 714–726.

75. Mundt, L. E.; Tong, J.; Palmstrom, A. F.; Dunfield, S. P.; Zhu, K.; Berry, J. J.; Schelhas, L. T.; Ratcliff, E. L., Surface-activated corrosion in tin–lead halide perovskite solar cells. *ACS Energy Lett.* **2020**, *5*, 3344–3351.

76. Ramadan, A. J.; Ralaiarisoa, M.; Zu, F.; Rochford, L. A.; Wenger, B.; Koch, N.; Snaith, H. J., Revealing the stoichiometric tolerance of lead trihalide perovskite thin films. *Chem. Mater.* **2020**, *32*, 114–120.

77. Azpiroz, J. M.; Mosconi, E.; Bisquert, J.; De Angelis, F., Defect migration in methylammonium lead iodide and its role in perovskite solar cell operation. *Energy Environ. Sci.* **2015**, *8*, 2118–2127.

78. Wang, J.; Yin, W.-J., Revisiting the iodine vacancy surface defects to rationalize passivation strategies in perovskite solar cells. *J. Phys. Chem. Lett.* **2022**, *13*, 6694–6700.

79. Pedersen, A.; Luisier, M., Lithiation of tin oxide: a computational study. *ACS Appl. Mater. Interfaces* **2014**, *6*, 22257–22263.

Synergistic surface modification of the mixed Sn–Pb perovskite films by the combination of piperazine and C_{60} pyrrolidine tris-acid realizes the power conversion efficiencies of the resultant solar cells up to 22.7% with substantially elongated life.

Shuaifeng Hu, Pei Zhao, Kyohei Nakano, Robert D. J. Oliver, Jorge Pascual, Joel A. Smith, Takumi Yamada, Minh Anh Truong, Richard Murdey, Nobutaka Shioya, Takeshi Hasegawa, Masahiro Ehara, Michael B. Johnston, Keisuke Tajima, Yoshihiko Kanemitsu, Henry J. Snaith, and Atsushi Wakamiya**

Synergistic Surface Modification of Tin–Lead Perovskite Solar Cells